JOURNAL OF SPACECRAFT AND ROCKETS
Vol. 47, No. 1, January–February 2010

Spacecraft Coating-Induced Charging: A Materials and Modeling Study of Environmental Extremes

Michelle M. Donegan* and Jennifer L. Sample†
Johns Hopkins University Applied Physics Laboratory, Laurel, Maryland 20723
and
J. R. Dennison‡ and Ryan Hoffmann§
Utah State University, Logan, Utah 84325

DOI: 10.2514/1.40882

As mankind reaches to explore extreme environments in space, the application of ceramics surface coatings is increasing. The 2005 mission concept for Solar Probe used a unique design to achieve the necessary thermal control for a very close approach to the solar corona, including the use of a highly refractory, electrically insulating ceramic coating over a carbon–carbon composite heat shield. The proposed trajectory takes the spacecraft from a Jovian fly-by to within 4 solar radii of the sun, spanning 5 orders of magnitude in solar radiation and solar wind plasma density as well as spacecraft temperatures from <100 K to >2000 K. Using the NASCAP-2K charging modeling program, the degree of charging expected for this spacecraft design has been calculated for this range of radiation environments. New measurements of the electron emission and estimates of related properties of the candidate materials, Al_2O_3, pyrolytic born nitride, and barium zirconium phosphate, are presented. Absolute and differential surface charging are found to depend strongly on temperature through increased conductivity at higher temperatures and on radiation flux through enhanced charge accumulation and radiation-induced conductivity. As the spacecraft approaches the sun, the competition between increased charge dissipation at higher temperatures and increased charge accumulation at higher fluxes leads to a maximum in differential charging between 0.2 and 2 astronomical units. Although the spacecraft charging behavior of these materials is found to be significant, it is not severe enough to endanger the mission, and a number of options exist to mitigate the degree of charging. Among the ceramics considered, the use of Al_2O_3 coatings is found to minimize both absolute and differential spacecraft charging.

Nomenclature

AU	=	astronomical unit $= 1.496 \times 10^8$ km
b_1, b_2	=	secondary electron range magnitudes
$\dot{D}$, $\dot{D}_{\text{photon}}$	=	electron and photon dose rates
E_0	=	activation energy related to trap energy depth below the conduction band edge
$E_{\max}$	=	energy at which maximum secondary emission $\delta_{\max}$ occurs
$E_{\text{inc}}^{\text{el}}$	=	incident electron energy
$J_{\text{emit}}^{\text{BSE}}$	=	emitted current due to backscattered electron emission
$J_{\text{inc}}^{\text{el}}$, $J_{\text{inc}}^{\text{ions}}$	=	incident electron and ion currents
$J_{\text{emit}}^{\text{ion}}$, $J_{\text{emit}}^{\text{photo}}$	=	emitted current due to ion-induced and photon-induced secondary electron emission
$J_{\text{emit}}^{\text{SE}}$	=	emitted current due to electron-induced secondary electron emission
J_{net}	=	net current
k_{RIC}	=	radiation-induced conductivity proportionality constant
n_1, n_2	=	secondary electron range exponents
n_e	=	electron number density
q_e	=	magnitude of electron charge
R, R_{photon}	=	incident electron and photon ranges
R_J	=	radius of Jupiter $= 6.991 \times 10^4$ km
R_S	=	radius of the sun $= 6.960 \times 10^5$ km
r	=	heliocentric distance from the sun
T	=	temperature
T_e, T_p	=	electron and proton temperatures
T_{eff}	=	effective plasma temperature
$Y_{\text{eh}}^{\text{photon}}$	=	electron-hole pairs created per absorbed photon
$\alpha_S/\varepsilon_{\text{IR}}$	=	solar absorptivity-to-infrared emissivity ratio
$\delta_{\max}$	=	maximum secondary electron yield
Δ	=	radiation-induced conductivity exponent
ε_r	=	relative dielectric constant
$\Psi_{\text{inc}}^{\text{photon}}$	=	incident photon flux
ρ_m	=	mass density
σ_{DC}, σ_{RIC}	=	dark current and radiation-induced conductivities
Θ	=	apex half-angle of heat shield cone
ν_{photon}	=	photon frequency

Received 15 January 2009; accepted for publication 2 September 2009.

*Senior Research Physicist, Milton Eisenhower Research Center, 11100 Johns Hopkins Road, Mail Stop 21-N348. Member AIAA.
†Senior Research Chemist, Milton Eisenhower Research Center, 11100 Johns Hopkins Road, Mail Stop 21-N109.
‡Professor, Physics Department, UMC 4415. Senior Member AIAA.
§Research Associate and Graduate Student, Physics Department, UMC 4415. Member AIAA.

I. Introduction

SPACECRAFT charging is caused by the interaction of the spacecraft with the space environment plasma. Electrically insulating materials are not typically used as coatings on spacecraft, and the phenomenon of environmental-induced charging of such materials has not been studied extensively. The Solar Probe mission proposed in 2005 [1], which would encounter temperatures as high as 2100 K at closest approach, requires a unique design to address the problem of thermal management [2,3]. The proposed solution included a cone-shaped primary heat shield that is composed of a carbon–carbon (CC) composite and coated with a thin layer of ceramic material (white surfaces, Fig. 1), the base of the cone and struts (gray surfaces) made of graphite materials, and the spacecraft

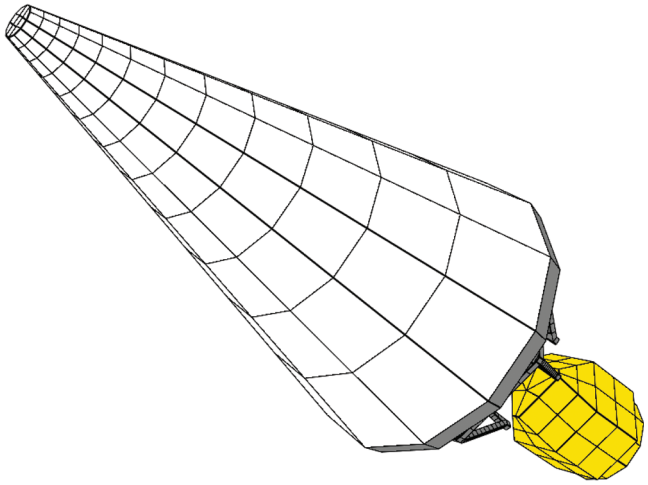

Fig. 1 Model of the proposed Solar Probe spacecraft design with a cone-shaped, ceramic-coated primary heat shield. The cone (white) is made of carbon-carbon coated composite material with a thin, insulating ceramic coating. The base of the cone and struts (gray) are conductive graphite material. The spacecraft bus (gold) is conductive black Kapton.

bus (gold surfaces) covered with conductive black Kapton [4]. Although the work presented here was performed as part of the 2005 Solar Probe concept, much of it has applicability to the current Solar Probe Plus concept [5,6].

The proposed (2005) mission would obtain a gravity assist from Jupiter, propelling the spacecraft to high solar latitudes such that it would approach the sun at the pole [1]. After closest approach, at ~4 solar radii, it would then enter a free-return trajectory taking it back out of the ecliptic plane, with aphelion at about 5 astronomical units (AU). Therefore, it was necessary to study the charging problem in multiple environments, including the approach to the sun, the closest approach, the Jovian environment, and interplanetary space. The proposed trajectory would subject the spacecraft to wide ranging environmental extremes including variations of more than 5 orders of magnitude in solar radiation and solar wind particle fluxes, the harsh high-energy Jovian magnetospheric plasma environment, and spacecraft heat shield equilibrium temperatures from <100 K to >2000 K. Survival of such extremes demands heat shield materials with specific properties.

The candidate coating materials were first selected based on their optical properties: the ideal coatings would enable survivability and mission feasibility by lowering the equilibrium temperature of the heat shield at closest approach [5]. Such materials are highly reflective, particularly in the visible and near-infrared, and either emissive thermally or are made into thermal windows passing thermal emission from the underlying CC composite [4]. Several ceramics were found to be well suited for this purpose and robust at the anticipated closest approach temperatures (~1600–2000 K). However, these materials are electrical insulators at room temperature; thus, careful analysis of their response and anticipated charging in the representative radiation environments encountered during the mission was required. It was necessary to understand the effects of the proposed ceramic coatings material properties on currents into and out of the spacecraft and how they would affect spacecraft charging.

Spacecraft surface net charge accumulation is a flux process as shown in Eq. (1), where J_{net} is the net current, $J_{\text{inc}}^{\text{el}}$ is the incident electron current, $J_{\text{inc}}^{\text{ions}}$ is the incident ion current, $J_{\text{emit}}^{\text{SE}}$ is the current out due to electron-induced secondary electron emission, $J_{\text{emit}}^{\text{BSE}}$ is the current out due to backscattered electron emission, $J_{\text{emit}}^{\text{ion}}$ is the current out due to ion-induced secondary electron emission, and $J_{\text{emit}}^{\text{photo}}$ is the current out due to photoemission

$$J_{\text{net}} = \left[J_{\text{inc}}^{\text{el}} + J_{\text{inc}}^{\text{ions}}\right] - \left[J_{\text{emit}}^{\text{SE}} + J_{\text{emit}}^{\text{BSE}} + J_{\text{emit}}^{\text{ions}} + J_{\text{emit}}^{\text{photo}}\right] \quad (1)$$

Note that in our convention electron currents are negative due to the sign of the charge carrier.

At equilibrium, $J_{\text{net}} = 0$, such that the current into the spacecraft (in the form of incident ions and electrons) equals the current out of the spacecraft (due to photoemission, secondary electron emission, and backscattered electrons) such that a potential develops relative to the surrounding plasma ground. Absolute charging develops when the local ground of the entire spacecraft charges relative to the plasma ground. Differential charging develops when different parts of the spacecraft charge to different potentials relative to one another. For example, consider a situation where one portion of the spacecraft (e.g., the heat shield) is exposed to the sun and this exposed surface experiences photoemission (leading to a net positive charge), whereas another electrically isolated and shaded portion without photoemission (e.g., the spacecraft bus), would develop a less positive potential leading to differential charging.

This study focuses on spacecraft surface charging. Such surface charging is typically expressed in terms of surface potential. For the Solar Probe mission, the primary charging-related concern deals with the electric field in the region surrounding the spacecraft that is produced by the potential on the spacecraft. Charging-induced changes to the electric field could cause instruments on a spacecraft to be unable to measure the true, uninfluenced electric field. Furthermore, this altered electric field influences the trajectories of incident charged particles, thereby compromising measurements of low-energy electrons and ions [7]. Because electric field and charged particle measurements are central to the science mission of Solar Probe, it is important to understand to what extent the spacecraft would charge during the mission and especially in the near-solar environment, where primary measurements would be made.

Internal charge accumulation and possible concomitant electrostatic discharge due to deep dielectric charging are not considered here. The cumulative flux of electrons greater than ~50 keV, which are typically said to cause deep dielectric, as opposed to surface, charging, is $\sim 10^{-4}$ of the total incident electron flux for solar wind with T_e of ~70 eV at 0.1 AU, is reduced by another factor of $>10^3$ at 0.2 AU with T_e of ~40 eV, and is many orders of magnitude further reduced at all other near-sun and deep-space trajectory points where $T_e < 35$ eV. At ≤ 0.2 AU, the heat shield temperature is large enough that enhanced dark current conductivity will probably dissipate the deep dielectric charge, although this situation should be considered in more detail to confirm this conjecture. Deep dielectric charging could be more important for the relatively brief period the spacecraft would spend in the Jovian magnetospheric environment. In this environment the electron temperature is greatly elevated, which enhances the magnitude of deep dielectric charging. Furthermore, the heat shield temperature is greatly reduced, inhibiting dark current conductivity.

Surface charging simulations were performed using the comprehensive NASCAP-2K charging analysis package. NASCAP-2K was developed by Science Applications International Corporation, NASA, and the Air Force for the purpose of modeling spacecraft potentials. This package was used to assess the expected charging of the spacecraft in the spacecraft's anticipated radiation environments. The NASCAP-2K solver uses a boundary element method algorithm to compute potentials over a nested grid structure [8,9]. Davis et al. [10] describe the validation of the NASCAP-2K solver's output . The solver requires three types of inputs: the geometry of the spacecraft, the radiation environment to which the spacecraft is subject, and material properties of the spacecraft components (see Fig. 2).

In this paper we will describe an assessment of the charging of the spacecraft in the anticipated radiation environments and for the candidate ceramic materials. We will first outline the methods for building a model of the spacecraft's geometry and estimating the radiation environment. We will present new measurements of the secondary and backscattered electron emission of three low absorptivity, high-yield, high-resistivity ceramic materials: alumina (Al_2O_3), pyrolytic boron nitride (PBN), and barium zirconium phosphate (BaZP). Methods used to estimate the temperature and flux dependence of other related materials properties will be discussed. Finally, we will discuss the results of the charging analysis in several different radiation environments.

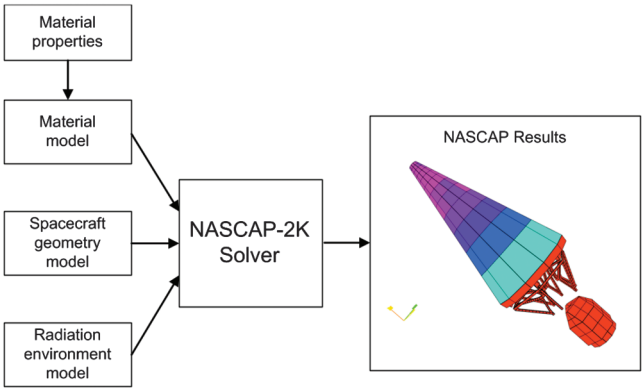

Fig. 2 Inputs to the NASCAP-2K charging solver.

II. Radiation and Plasma Environment Definition

The trajectory for the 2005 Solar Probe concept [1,11] had the spacecraft spend about 28 days in close proximity to the sun. Because the nominal start-of-science point is 0.3 AU, the charging problem was considered beginning at a distance of 0.5 AU from the sun. The remaining 7–8 years of the mission would be spent in the Jovian and deep-space environments out to the perigee of Jupiter at ~5 AU. The spacecraft would need to survive those environments; although it would not be conducting science operations there, it would need to remain in contact with Earth during these time periods.

The near-sun environment features large electron and ion plasma densities, whereas by contrast, the densities are several orders of magnitude lower in deep space. The near-sun and deep-space environments are modeled with a Maxwellian distribution of electrons plus a beam of solar wind ions [12], and the Jovian environment is modeled by a double Maxwellian distribution to include both the hot and cold plasma components [13]. The Jovian case includes much higher electron and ion temperatures than the other situations. Relatively large solar radiation intensities are another feature of the near-sun environment; the large magnitude of blackbody (primarily infrared) radiation in the solar spectrum led to the decision to use a ceramic coating with low absorptivity α in the infrared in the design to minimize spacecraft heating, whereas the high-intensity ultraviolet and visible radiation at energies sufficient for photoelectron generation (mainly from the hydrogen Lyman-α emission at 10.2 eV) leading to high photoemission is minimized by choosing ceramic coatings with higher emissivity ε in the ultraviolet and visible range. In general, charging is dominated by electron processes. Negative charging is induced by electron bombardment, and secondary electron emission and photoemission, and to a much lesser extent backscattered and ion-induced secondary electron emission, contributes to positive charging [14]. The combination of these processes establishes the current balance over the spacecraft.

The radiation environments that the spacecraft was anticipated to experience, particularly the near-sun environments, are not well understood at this time. No spacecraft has yet ventured inside 0.3 AU (the perihelion of the Helios probes) [15], and only Ulysses has provided any data on the solar wind conditions out of the ecliptic plane [12,16]. It was therefore necessary to attempt to model the very environment that Solar Probe would study. For the purposes of the charging study, reasonable estimates of radiation environments were made using published measured data in the literature along with published simulations and discussions with radiation environment experts.

The Solar Probe trajectory uses a Jupiter gravity assist to slingshot out of the ecliptic plane such that it approaches the sun from its north pole. Because of its solar polar orbit, Solar Probe was planned to traverse solar wind environments ranging from the high-latitude polar regions to low-latitude equatorial regions. A number of studies have used data from Helios, Ulysses, and other solar-observing spacecraft to model the temperature gradients and plasma environments over a wide range of distances from the sun. Polar plasma parameters for the range 0.1–0.5 AU were calculated from such models in literature. The electron temperature was calculated using the power law model $T_e \sim r^{\beta}$ of Maksimovic et al. [17], which gives fits to binned Ulysses data of $(1.33 \times 10^5) r^{-0.78 \pm 0.21}$ K for the solar south pole and $(1.28 \times 10^5) r^{-0.868 \pm 0.21}$ K for the solar north pole. The ion temperatures were calculated using the model of Guhathakurta et al. [18] and $T_{\text{eff}} = (T_e + T_p)/2$. Plasma densities were computed from Helios data according to the assumption that $n_e \sim r^{-2}$ [18]. It was assumed that the plasma is neutral on the macroscopic scale such that the proton density is equal to that of electrons. For the temperature at the closest approach point at $4R_S$, we have extrapolated backward from the base of the corona ($1.03R_S$) with a temperature of 1 MK. The plasma densities were calculated as for the 0.1–0.5 AU cases [19]. The parameters for the two deep-space trajectory points and for the Jovian environment were also obtained from the literature [13,18–26]. The plasma radiation environment parameters used for our simulations for near-sun and deep-space trajectory points are given in Table 1 and illustrated graphically in Fig. 3, and those for Jovian environments are listed in Table 2.

NASCAP calculations assume that the relative solar radiation intensities as a function of wavelength are the same as for the standard solar spectrum at 1 AU [8,27]. Tables 1 and 2, and Fig. 3 show the incident solar intensity that scales as r^{-2} as a function of distance from the sun for the various environments, where one sun is defined as the integrated solar intensity at 1 AU.

III. Materials Properties

The electron emission and transport properties of materials are key parameters in determining the likelihood of deleterious spacecraft charging effects, and are essential in modeling these effects with engineering tools such as the NASA NASCAP-2K code. Surface charging results primarily from keV electron fluxes and photoemission, whereas deep dielectric charging is usually caused by high-energy electron and proton fluxes from the trapped radiation. Accumulation and reemission of electron, ion, and photon fluxes in space determine charge accumulation. Dissipation or redistribution of this accumulated charge throughout a spacecraft is governed primarily by the conductivity of high-resistivity components of the spacecraft [3,12,28]. In turn, conductivity is substantially affected by the charge and energy deposited by the incident radiation fluxes, which modify the electric field stress, temperature, and absorbed radiation energy dose of the material.

The potential that develops on a spacecraft surface results from the processes delineated by Eq. (1). Each factor in this equation depends on the radiation environment and the material properties that govern emission and charge transport. Although spacecraft charging can be investigated computationally and predicted using available software programs such as NASCAP-2K, accurate radiation environment definition and material properties are integral to ensuring the integrity of the results. As discussed in Sec. II, radiation environment and expected photon intensity can often be determined using a combination of data available from previous space exploration missions and scaling laws. The material properties governing charging for many common spacecraft materials such as aluminum and Kapton are well understood [27–29]. For example, previous studies have measured materials properties and determined appropriate parameters for NASCAP fits for materials such as graphite (used in the base of the spacecraft cone and struts) and black Kapton (spacecraft bus) [30]. When these data are unavailable, as was the case here for the proposed ceramic Solar Probe coatings, they must be measured to appropriately model charging effects.

A. Description of Materials

Conventional materials used for spacecraft outer surfaces (aluminum, metalized Kapton, etc.) are conductive, thereby preventing the buildup of differential charge, as charge can dissipate across the entire surface between conductive materials assuming proper local grounding. The extremely high temperatures that Solar Probe would encounter during the 2005 planned solar approach required the use of refractory ceramic materials as a component of the passive thermal management system, chosen because of their outstanding

Table 1 Radiation environment parameters for Solar Probe spacecraft trajectory points

Parameter	Near sun					Deep space			
	$4R_S$	0.1 AU	0.2 AU	0.3 AU	0.4 AU	0.5 AU	2.5 AU	5.0 AU
Spacecraft latitude (°)	0	50	35	28	24	21	0	0
Plasma number density (m^{-3})	$(2.35 \pm 0.03) \times 10^{10}$	$(3.2 \pm 0.3) \times 10^{8}$	$(7.9 \pm 0.8) \times 10^{7}$	$(3.5 \pm 0.4) \times 10^{7}$	$(2.0 \pm 0.2) \times 10^{7}$	$(1.3 \pm 0.1) \times 10^{7}$	$(4.8 \pm 0.5) \times 10^{5}$	$(1.2 \pm 0.1) \times 10^{5}$
Isotropic current density (nA-cm^{-2})	1.2×10^{3}	24	4.5	1.7	0.84	0.51	8.7×10^{-3}	1.9×10^{3}
Electron temperature, eV	34.6 (+9.6,–7.5)	74 (+47, −28)	42 (+17, −12)	30 (+9, −7)	23 (+5, −4)	20 ± 3	4.3 (+1.9, −0.1)	3.4 (+0.7, −1.3)
Electron range, nm	2	2	2	2	3	3	28	45
Electron dose rate, Rad-s^{-1}	6.1×10^{6}	2.4×10^{5}	2.7×10^{4}	6.9×10^{3}	2.0×10^{3}	9.2×10^{2}	3.5×10^{-1}	3.8×10^{-2}
Ion beam velocity, km/s	440	750	750	700	600	550	440	440
Solar intensity (number of suns)	2887	100	25	11.1	6.25	4	0.16	0.04
Heat shield temperature, K, $\alpha_S/\varepsilon_{IR} = 0.6$	1850	798	564	460	399	357	<100	<100
Heat shield temperature, K, $\alpha_S/\varepsilon_{IR} = 0.2$	—	594	410	343	292	271	—	—

optical properties (very low solar absorptivity-to-infrared emissivity ratio $\alpha_S/\varepsilon_{IR}$), refractory nature, and chemical and processing compatibility with other spacecraft materials [4]. Their ability to reflect incident solar irradiance and emit thermal energy could enhance mission success by decreasing the equilibrium temperature of the primary shield, which in turn decreases launch mass and costs. The optical properties decreased the equilibrium operating temperature of the heat shield by 300–500 K.

The baseline coating for the Solar Probe primary shield (without modifications such as doping) is a thin (100–125 μm) coating of alumina Al_2O_3 on a CC composite. Two other coating materials also were under consideration, PBN and BaZP. Many of the ceramics tested and reported here were deposited onto CC composite coupons, which is the projected substrate and base heat shield material for the spacecraft. The materials were deposited either by plasma spray deposition or chemical vapor deposition to the desired thickness. Information about this process and the resulting ceramic microstructure can be found elsewhere [31]. All materials are known or estimated to have very high electrical resistivity at room temperature ($\sim 10^{15}$ ohm · cm) [32–35]. They become more electrically conductive with increasing temperature, allowing rapid charge dissipation at the very high temperatures expected near perihelion (spacecraft closest approach). Because ceramics are typically electrically insulating and therefore tend to collect surface charge at room temperature and at low radiation dose, special attention was devoted to understanding how their electronic properties vary at selected points along the Solar Probe trajectory and how their interaction with the radiation environment could affect the overall spacecraft charging.

B. NASCAP Materials Parameters

The NASCAP-2K code [8] uses parameterized expressions to represent the materials properties involved in charge accumulation and dissipation, including 1) electron-, ion-, and photon-induced electron emission yields, 2) mass density, 3) dielectric constant, 4) electrostatic breakdown potentials and field strengths, and 5) both dark current and radiation-induced electron conduction [36]. Total conductivity is the sum of two temperature-dependent material properties, dark current conductivity, which is independent of the incident radiation, and radiation-induced conductivity (RIC), which by definition is conductivity enhanced by the energy imparted to a material by the incident radiation [37]. The NASCAP parameterization does not model temperature dependence of these parameters, so specific values of the materials parameters must be input into the code for the equilibrium temperatures in each environment listed in Tables 1 and 2.

Many of these materials properties have been measured for this study, others are available in the literature, and some are not available at all. The text in the next two subsections describes how the appropriate NASCAP parameters for materials properties are determined or approximated for use in the calculations in Sec. IV. Parameter values used for Al_2O_3, PBN, and BaZP are listed in Table 3.

C. Electron Emission Properties

Measurements of the electron-induced electron emission properties of Al_2O_3, PBN, and BaZP were made by the Materials Physics Group at Utah State University (USU) [30,38,39]. Accurate absolute electron yield measurements are more difficult to make on dielectrics than on conductors, because any charge that is deposited in the material is not highly mobile and cannot easily be neutralized [40]. The tests employed low-fluence capabilities for testing high-yield, extremely high-resistivity materials using a pulsed yield system with alternating charge neutralization and a charge decay curve method to make reliable and reproducible measurements of the absolute total yield curves [39,40]. The direct-current and pulsed-electron yield methods used here are described fully elsewhere [38,39]. The electron yield curve shows electrons emitted from a material as a function of incident electron energy and provides a measure of the number of electrons emitted for each incident electron on a material. For electron yields greater than unity, a material emits more electrons

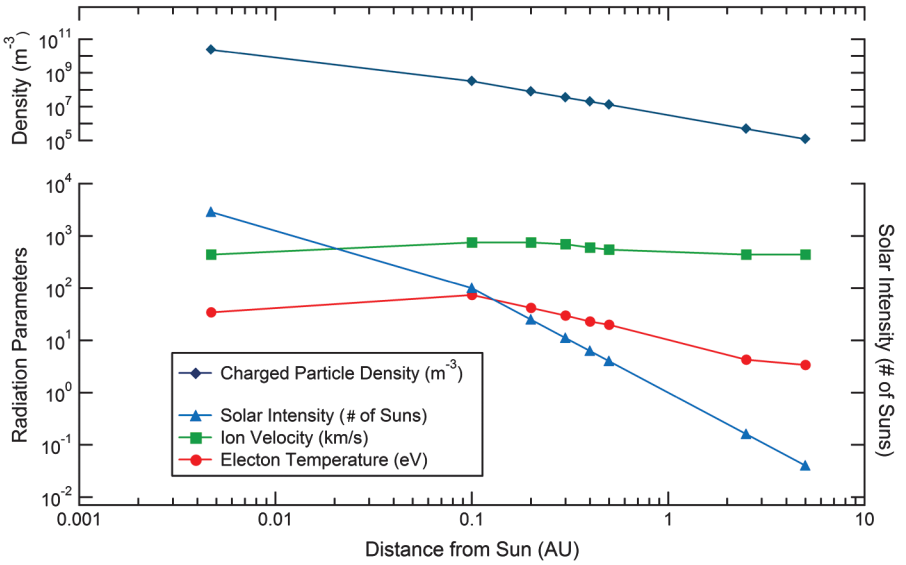

Fig. 3 Radiation environment parameters for near-sun and deep-space trajectory points. The plasma number densities are plotted as black diamonds in the upper graph. The electron temperature and ion beam velocity are plotted as red circles and green squares, respectively, along the lower left-hand axis. The solar intensity is plotted as blue triangles along the lower right-hand axis.

than are bombarding it and it may acquire a positive rather than a negative charge even in an electron environment, depending on the distribution of radiation fluxes and energies.

Figure 4 shows the measured secondary and backscattered electron yield of Al_2O_3 at room temperature (298 ± 3 K) for incident electrons from 20 eV to 20 keV [41]. Table 3 lists the parameters for fits to the data shown in Fig. 4, using a NASCAP five parameter fit for secondary yields and a NASCAP one parameter fit for backscattered yields [8,39]. Parameters for secondary electron emission required for NASCAP include the maximum electron yield δ_{max}, the energy E_{max} at δ_{max}, and magnitudes and exponents for a dual power law model of the stopping power, n_1, b_1, n_2, and b_2 [8,39]. Note that only the ratio b_2/b_1 is relevant for NASCAP [39,42]. Pronounced effects of charging of Al_2O_3 on the yield are evident by the depressed yield observed between incident energies of ~200 eV to ~1100 eV (shaded region in Fig. 4). The corrected intrinsic yield for uncharged material determined by yield decay curve extrapolation to zero surface potential is in very good agreement with yield measurements made on a different type of polycrystalline Al_2O_3 at an undetermined higher temperature and higher dose rate where resistivity is much lower and charge is more readily dissipated [43]. A USU measurement at 348 ± 5 K also found no appreciable change in yield from the 298 K data in Fig. 4.

Table 2 Radiation environment parameters for the near-Jovian trajectory point

Parameter	Jupiter $12R_J$	
	$12R_J$ (double Maxwellian)	
Electron number density, m^{-3}	2.0 (+2.0, −1.0) × 10^5	1.2 (+1.2, −0.6) × 10^6
Isotropic current density, nA-cm^{-2}	7.4 × 10^{-2}	1.9
Electron temperature, eV	200 (+200, ±80)	2.8 (+2.8, −2.2) × 10^4
Electron range, nm	4	5000
Electron dose rate, Rad-s^{-1}	9.2 × 10^2	2.8 × 10^3
Ion number density, m^{-3}	6.0 (+6.0, −3.0) × 10^5	1.3 (+1.3, −0.6) × 10^6
Ion temperature, eV	400 (+400, −350)	2.8 (+2.8, −2.2) × 10^4
Solar intensity (number of suns)	0.033	
Heat shield temperature, K, $\alpha_S/\varepsilon_{IR} = 0.6$	<100	

Similar measurements of electron emission secondary and backscattered yields were made for PBN and BaZP; fitting parameters are listed in Table 3. Both materials exhibited suppressed yields for incident energies from ~200 eV to ~2 keV, similar to Al_2O_3. Maximum yields at ~680 eV were estimated to be 7.0 ± 0.6 and 5.0 ± 0.5 for PBN and BaZP, respectively. BaZP displayed extreme charging as evidenced by its erratic emission data as a function of incident energy, with very long discharge times (up to 5 days) [44]. Because BaZP is a relatively new material having little material property data publicly available in the literature, these results were particularly valuable, providing insight into unknown properties such as dielectric constant and dark current or radiation-induced conductivities and allowing refinement of coating material candidate choices.

The ion-induced electron yields of Al_2O_3 have been measured for incident heavier ions (Li to Cs) from 90 eV to 29 keV [45]. Both theory and results of Dietz and Sheffield [45] show that ion yield scales approximately as the square root of the incident ion mass. The fitting parameters are listed in Table 3 for a two parameter fit to H ion yield used in NASCAP-2K, fit to the Dietz Li^6 data scaled by the square root of the H:Li mass ratio 0.41. There is no information about the temperature dependence of ion yield values. Ion yield scales only weakly with target mean atomic number (10, 6, and 14.2 for Al_2O_3, PBN, and BaZP, respectively) and Dietz finds <30% variation in Li yields for the ceramic metal oxides BeO, Al_2O_3, MgO, and Ta_2O_5 with a range of atomic number from 6 to ~26. Given this and the fact that ion-induced emissions typically contribute much less to spacecraft charging than electron yields or photoyields, it is reasonable to use these Al_2O_3 ion yields as surrogates to model PBN and BaZP.

Photoyields for photon energies from <1 eV to ~25 eV were measured for Al_2O_3 [46] and convoluted with the standard solar flux energy spectrum to determine the differential photoelectron flux versus incident photon energy under perpendicular solar irradiation [47]. This integrated total photoelectron yield for the normal incident solar spectrum (that is, the total number of electrons emitted for normal solar light per unit area per unit time) for Al_2O_3, $4.20 \cdot 10^{-5}$ A/m^2 is the sole parameter used in NASCAP-2K to describe photoemission from an incident solar flux spectrum at a distance of 1 AU from the sun just above the Earth's atmosphere. This photoyield value depends appreciably on the absorptivity, angle of incidence, surface roughness, and contamination or surface degradation [48,49]. Values for the mean absorptivity over a wavelength range of 250–750 nm can be estimated from measured room-temperature reflectivity curves, assuming $\bar{\alpha} = 1 - \bar{R}$ for the Feurerbacher data [46] as $\alpha_{Al_2O_3} \approx 0.15$ and for the Solar Probe samples as $\alpha_{Al_2O_3} \approx 0.27$, $\alpha_{PBN} \approx 0.33$, and $\alpha_{BaZP} \approx 0.28$ [4].

Table 3 Ceramic material property parameters determined for use in NASCAP simulations

Property	Parameter	Units	Heat shield material		
			Al_2O_3	PBN	BaZP
Density	Room-temperature value, ρ_m	kg-m^{-3}	3.83×10^3	2.20×10^3	2.43×10^3
Dielectric properties					
Relative dielectric constant	Room-temperature value, ε_r	unitless	14.9	4.2	4.2
	Temperature coefficient, Δ_ε	K^{-1}	2.0×10^{-3}	1.5×10^{-4}	1.5×10^{-4}
Dielectric field strength	Electrostatic field strength at room temperature, E_{ESD}^{RT}	MV-m^{-1}	27.4	37.4	27.4
	Temperature coefficient, α_{ESD}	K^{-1}	2.8×10^{-3}	2.8×10^{-3}	2.8×10^{-3}
Dark current conductivity	Conduction coefficient, σ_o^{DC}	$(\Omega\text{-cm})^{-1}$	3×10^0	1×10^1	3×10^0
	Activation energy, E_o	eV	0.75	0.85	0.75
Radiation-induced conductivity	RIC coefficient, k_{RICo}	$(\Omega\text{-cm-Rad-s}^{-1})^{-1}$	6×10^{-9}	6×10^{-9}	6×10^{-9}
	RIC coefficient, k_{RICo}	unitless	1×10^{-8}	1×10^{-8}	1×10^{-8}
	RIC power, T_R	K	1800	1800	1800
Electron emission					
Secondary yield	Maximum yield, $\delta_{\max}$	unitless	6.4 ± 0.2	7.0 ± 0.5	5.0 ± 0.6
	Energy at $\delta_{\max}$, $E_{\max}$	keV	0.45 ± 0.05	0.65 ± 0.03	0.70 ± 0.03
	Range coefficient, b_1	Å	5 ± 1	6 ± 2	0.2 ± 0.1
	Range power, n_1	unitless	0.1 ± 0.01	0.6 ± 0.2	0.6 ± 0.3
	Range coefficient, b_2	Å	1	1	1
	Range power, n_2	unitless	2.5 ± 0.1	3.0 ± 0.2	3.2 ± 0.3
Backscattered yield	Effective atomic number, Z_{eff}	unitless	10.2 ± 2	6.3 ± 1	23.7 ± 3
Ion yield	H^+ yield at 1 keV, $\Gamma_{1\,\mathrm{kV}}$	unitless	0.68	0.68	0.68
	Energy at max H^+ yield, $E_{H\max}$	keV	60	60	60
Integrated photoyield	Total photoyield at ≤ 1 AU, Y_{photo}	A-m^{-2}	7.6×10^{-5}	9.2×10^{-5}	7.8×10^{-5}

[a]Methods used to determine parameter values are discussed in detail in the text

The photoyield is also expected to have some temperature dependence, as is the absorptivity [4,48]. Given these uncertainties and variabilities of the materials during the mission lifetime, it is a reasonable approximation to use the value for Al_2O_3 photoyield (corrected for absorptivity ratios) as a surrogate for PBN and BaZP, because they are similar ceramic materials with roughly comparable optical absorptivity and band gaps. The corrections of the photoyield and absorptivity for grazing incidence [48,49] of the solar radiation on the heat shield cone with cone half-angle of $\Theta = 15$ deg have been included in the present calculations. The calculations take into account the following:

1) The photoyield current is proportional to the decrease in cross-sectional area with increasing angle of incidence [e.g., $J_{\mathrm{emit}}^{\mathrm{photo}} \sim \cos(1-\Theta)$], which is modeled in NASCAP.

2) The absorptivity decreases with increasing angle of incidence, because the reflectivity at grazing angle is increased; that is, $\alpha \sim 1/\cos(1-\Theta)$.

3) When the penetration depth of the photon exceeds the escape depth (range) of the low-energy photoelectrons produced in the material, the emission of fraction photoelectron produced near the surface that can escape is enhanced by a factor of $\cos(1-\Theta)$. However, when the photon penetration depth does not exceed the photoelectron escape depth, an approximately constant fraction of the photoelectrons escape independent of Θ.

In this case of deep photon penetration, as is true for the near-sun trajectory points, the terms (2) and (3) effectively cancel each other. However, for H Lyman α photons, which dominate the photoyield from the solar spectrum, the penetration depth $\sim$8 nm [50] is less than the escape depth for electrons [51] in the deep-space and Jovian environments (see Sec. III.D); in this case photoyield measured at normal incidence need be reduced by a factor of $1/\cos(1-\Theta)$ to account for (2), but to not correct for (3).

D. Electrostatic and Related Materials Properties

The measured densities at room temperature of Al_2O_3, PBN, and BaZP are listed in Table 3. Measured values for Al_2O_3 and PBN agreed with manufacturers values [32–34,52] to within <1%. No

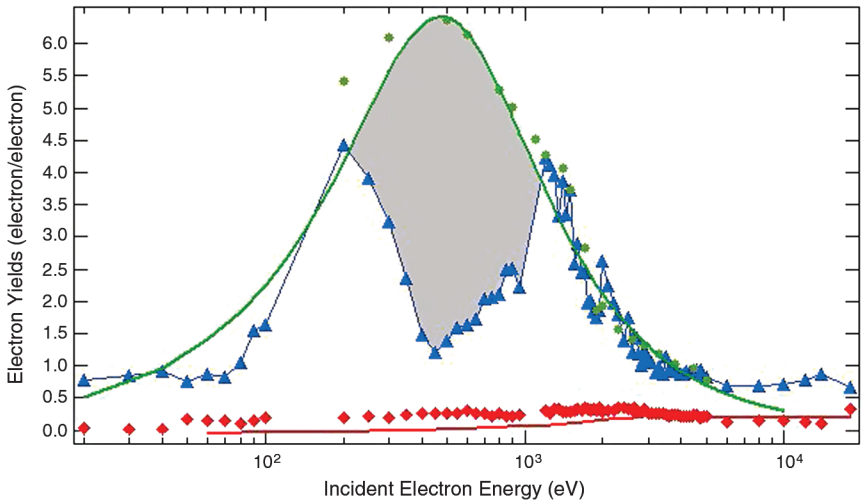

Fig. 4 Electron emission yield as a function of incident electron energy for polycrystalline Al_2O_3. Pulsed yield measurements of secondary electron yields (blue triangles) and backscattered yields (red diamonds) are shown. Dashed green curve shows a NASCAP 5 parameter fit of the secondary yield including points (green circles) determined by yield decay curve extrapolation to zero surface potential. Dashed purple line shows a NASCAP one parameter fit to the backscattered yield. Fitting parameters are listed in Table 3.

values for the density of BaZP were found in the literature for comparison with our measurements. Variations in density with temperature were not considered here, as these ceramics all have relatively low thermal expansion coefficients [32–34,52].

The relative dielectric constants of Al_2O_3 and PBN were found to increase linearly with temperature, as

$$\varepsilon_r(T) = \varepsilon_{RT} + \Delta_\varepsilon(T - 298\ \mathrm{K}) \tag{2}$$

Δ_ε for Al_2O_3 was determined from an extensive data set by Morrell [35]; ε_{RT} for Al_2O_3, 14.9, was determined from a manufacturer's value [34] at room temperature for the specific form and purity of Al_2O_3 coating material (Al970CD) proposed for use in the Solar Probe spacecraft. The fitting parameters for PBN, which showed much smaller temperature variations, were determined from more limited data including an average bulk value at room temperature [32] and values along both the a and c crystal axes [33,34,52]. No data were available for the dielectric constant of BaZP; PBN values were used as surrogates because PBN had values more similar to other ceramics than those of Al_2O_3. The values for ε_r and Δ_ε used for Eq. (2) for the three materials are listed in Table 3.

The electrostatic field strength of Al_2O_3 was found to decrease exponentially with increasing temperature [32,35,53], following an empirical form found by other investigators [54], which is an approximate form [35] of the more complete expressions developed from multiple trapping theory [14,55]

$$E_{\mathrm{ESD}}(T) = E_{\mathrm{ESD}}^{RT} e^{-\alpha_{\mathrm{ESD}}(T - 298\ \mathrm{K})} \tag{3}$$

where the coefficient of linear temperature change derived from Al_2O_3 data, $\alpha_{\mathrm{ESD}} = (2.8 \cdot 10^{-3})\ \mathrm{K}^{-1}$ is used for all three materials and where E_{ESD}^{RT} is the electrostatic field strength at room temperature (listed for each material in Table 3). As an alternate expression for $E_{\mathrm{ESD}}(T)$, the most complete data set for Al_2O_3 from ~300 K to ~1800 K [35,53] can be scaled to the manufacturer's value of E_{ESD}^{RT} for either Al_2O_3 or PBN [13,32,34]. No data were available for the breakdown field strength of BaZP; Al_2O_3 values were used as surrogates because Al_2O_3 had values more similar to other ceramics than those of PBN. The values for E_{ESD}^{RT} and α_{ESD} used for Eq. (3) for the three materials are listed in Table 3.

Several available data sets of the dark current conductivity of Al_2O_3 as a function of temperature [32,35,52] showed a roughly exponential increase in conductivity with increasing T. These combined data sets were fit with an Arrhenius function of the form

$$\sigma_{\mathrm{DC}}(T) = \sigma_o^{\mathrm{DC}} e^{-E_o/k_B T} \tag{4}$$

as predicted by standard theories of thermally assisted conductivity of semiconductors and insulators at higher temperatures [56,57]. In such models, σ_o^{DC} sets the magnitude of the conductivity and E_{on} is an activation energy for electrons excited from localized trap states into the conduction band. The fit was scaled so that it has the manufacturer's conductivity value at room temperature (Morgan, type Al970CD) [34]. A plot of the conductivity of Al_2O_3 as a function of temperature used in the NASCAP modeling of surface voltage is shown in Fig. 5. Similar but less extensive data are available for the conductivity of PBN as a function of temperature [33,52]. No data were available for the resistivity of BaZP; Al_2O_3 values were used as surrogates. Values of the coefficients σ_o^{DC} and E_o for Eq. (4) are found in Table 3.

In addition to the thermally assisted conduction mechanisms for dark current conductivity, electrons can be excited into the conduction band by high-energy incident radiation and then thermally move in and out of trap states near the conduction band edge as they travel in the conduction band under the influence of an applied electric field [58–60]. This insulator conduction mechanism is referred to as radiation induced conductivity (RIC). RIC is given by a simple power law

$$\sigma_{\mathrm{RIC}}(T) = k_{\mathrm{RIC}}(T)\dot{D}^{\Delta(T)} \tag{5}$$

based on the Rose–Fowler multiple trapping model [58,59], where both the proportionality constant k_{RIC} and the exponent Δ can be

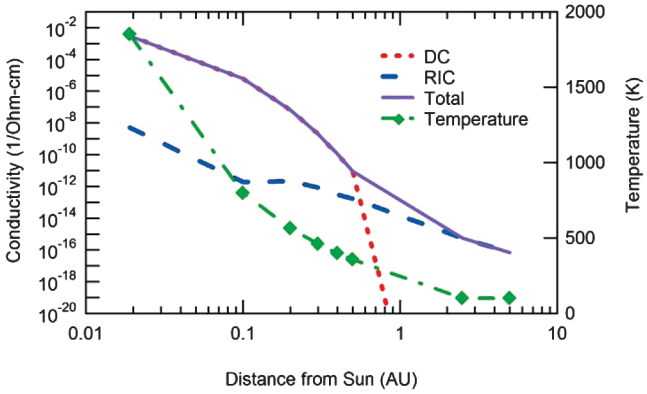

Fig. 5 Conductivity and heat shield temperature for Al_2O_3 with $\alpha_S/\varepsilon_{\mathrm{IR}} = 0.6$ as a function of spacecraft distance from the sun.

expressed as material dependent functions of T [7,60]. Temperature-dependent values of k_{RIC} and Δ over a range from ~290 K to ~1200 K can be derived from curves for Al_2O_3 presented in Klaffky [61]. Δ is ~1 below ~600 K, decreases to ~0.74 at 810 K, and asymptotically approaches 0.5 at higher temperatures, and k_{RIC} has a minimum value of $1.1 \cdot 10^{-16}\ (\Omega\text{-cm-Rad/s})^{-1}$ at ~630 K, increases roughly exponentially to $1.2 \cdot 10^{-14}\ (\Omega\text{-cm-Rad/s})^{-1}$ at 1220 K with increasing temperature, and increases roughly exponentially to $4.8 \cdot 16^{-16}\ (\Omega\text{-cm-Rad/s})^{-1}$ at 290 K with decreasing temperature. The observed temperature dependence of k_{RIC} and Δ is consistent with predictions based on the Rose–Fowler multiple trapping model [28,58,59]. Because there is no RIC data available for PBN or BaZP, the Al_2O_3 values were used as surrogates.

The dose rate in Eq. (5) $\dot{D}$ is defined as the total energy deposited in a material by the incident radiation per unit mass per unit time and is given approximately by [62]

$$\dot{D} = \frac{|J_{\mathrm{inc}}^{\mathrm{el}}|E_{\mathrm{inc}}^{\mathrm{el}}}{\rho_m q_e R} \tag{6}$$

where $J_{\mathrm{inc}}^{\mathrm{el}}$ and $E_{\mathrm{inc}}^{\mathrm{el}}$ are the incident electron current density and energy, and R is the range of the incident electron in the Bethe and continuous slow down approximations [63]. It is important to recognize that RIC will only produce enhanced charge transport within the upper layer of a dielectric coating to a depth R (see the following discussion), and will lead to charge dissipation only if this surface layer has a conduction path to areas of differential charge or a local ground. It will not significantly enhance the charge dissipation through the Solar Probe ceramic coating, with a thickness ~10^3 times the range of vast majority of electrons in the solar wind plasma, to the underlying conductive carbon–carbon composite substrate at spacecraft ground. $J_{\mathrm{inc}}^{\mathrm{el}}$ is determined from the electron number densities and electron temperatures listed in Tables 1 and 2, using the first moment of the Maxwellian velocity distribution [64]

$$J_{\mathrm{inc}}^{\mathrm{el}} = q_e n_e \bar{v}_{\mathrm{drift}} = \begin{cases} q_e n_e \sqrt{\frac{8k_B T_e}{\pi m_e}} & \text{for } 3D \text{ isotropic fluxes} \\ q_e n_e \sqrt{\frac{2k_B T_e}{\pi m_e}} & \text{for } 1D \text{ unidirectional fluxes} \end{cases} \tag{7}$$

The range [8,39] for Al_2O_3 at incident energies from 10^4 eV to 10^6 eV in the continuous slow down approximation is tabulated in the ESTAR database [51]. The ranges for PBN and BaZP in this energy interval are approximated by scaling the Al_2O_3 range data by the ratio of Al_2O_3 density to the PBN or BaZP density using the ESTAR database [51]. Direct extrapolation of the ESTAR data to lower energies is not valid for energies comparable to the atomic electronic structure, typically a few keV and below, because the discrete energy nature of the collisions becomes important. Instead, at low energies the range is approximated here by using the same density scaling of the product of a universal curve of electron mean free paths for conductors [65–67] times the probability an energy loss collision will occur, $\lfloor 1 - e^{-E_{\mathrm{inc}}^{\mathrm{el}}/E_{\min}} \rfloor$, times the mean number of

possible energy loss collisions $E_{\text{inc}}^{\text{el}}/E_{\min}$ where $E_{\min}$ is the mean energy lost by the incident electron per inelastic collision (approximately equal to the energy at the minimum mean free path in the universal curve).

In Solar Probe environments, the range of electrons at the peak energy of the solar wind plasma distribution at near-sun trajectory points varies from ~2 nm to 3 nm, at deep-space trajectory point from ~30 nm to ~50 nm; this modest change is expected because R scales as $E_{\text{inc}}^{\text{el}}$ and is independent of $J_{\text{inc}}^{\text{el}}$. In the high-energy Jovian environment, $R \sim 5000$ nm. The incident electron current scales as r^{-2} so large changes are expected over the near-sun and deep-space trajectory points; indeed $J_{\text{inc}}^{\text{el}}$ varies 6 orders of magnitude from 10^3 nA-cm^{-2} to 10^{-3} nA-cm^{-2}. The electron dose rate scales as the product $J_{\text{inc}}^{\text{el}} \cdot E_{\text{inc}}^{\text{el}}$, resulting in more than 8 orders of magnitude change from $>10^6$ Rad-s^{-1} to ~10^{-2} Rad-s^{-1} over the near-sun and deep-space trajectory points. Specific values of R, $E_{\text{inc}}^{\text{el}}$, $J_{\text{inc}}^{\text{el}}$, and $\dot{D}$ at the various trajectory points are listed in Tables 1–3.

As an aside, we offer a comment about an aspect of RIC that is not generally considered, RIC due to energy deposition for intense UV radiation. Measurements [68,69] on ceramic materials, including Al_2O_3, have demonstrated that vacuum ultraviolet (VUV) radiation in the range of ~8 eV to ~20 eV produces not only photoemission, but significantly enhances conductivity and charge dissipation of the charge produced by the photoemission that is approximately linearly proportional to VUV intensity. This occurs at energies somewhat greater than the material bandgap, and is attributed to electron-hole pair production. It can be thought of as photon-induced radiation conductivity of a form like Eq. (5) with an analogous photon dose rate given approximately by

$$\dot{D}_{\text{photon}} = \frac{Y_{\text{eh}}^{\text{photon}} \Psi_{\text{inc}}^{\text{photon}} (h\nu_{\text{photon}})}{\rho_m R_{\text{photon}}} \tag{8}$$

where $\Psi_{\text{inc}}^{\text{photon}}$ and $h\nu_{\text{photon}}$ are the absorbed photon flux and energy, and R_{photon} is the penetration depth (range) of the absorbed photon. $Y_{\text{eh}}^{\text{photon}}$ is the number of electron-hole pairs produced per absorbed photon; because the photoyield of Al_2O_3 is only ~0.08 photoelectrons/photon in the range 8 eV $< h\nu_{\text{photon}} <$ 25 eV [47], it is reasonable to expect $0.1 < Y_{\text{eh}}^{\text{photon}} < 1$, which is roughly consistent with observation [68,69]. The photon dose rate calculated from Eq. (6) for H Lyman α solar radiation (with $h\nu_{\text{photon}} = 10.2$ eV, $\Psi_{\text{inc}}^{\text{photon}} = 2.7 \cdot 10^{15}$ photons-m^{-2}-s^{-1} at 1 AU [47], $R_{\text{photon}} = 8$ nm, and $Y_{\text{eh}}^{\text{photon}} = 1$) is $1 \cdot 10^4$ Rad-s^{-1}, almost 10^4 times the dose rate from the electron plasma of the solar wind to a depth of ~20% of the low-energy electrons. This ratio would be expected to be constant for the range of trajectory distances, because the photon spectrum and T_e (approximately; see Fig. 3) are independent of r and both $\Psi_{\text{inc}}^{\text{photon}}$ and $J_{\text{inc}}^{\text{el}}$ are approximately proportional to r^{-2}, but the contribution from electrons will increase dramatically in environments like the Jovian one where T_e is increased substantially. Although the estimate of $\dot{D}_{\text{photon}}$ made here is rough at best, it is clear that further consideration is warranted to determine if this makes a significant contribution to the dissipation of charge on the ceramic coatings.

The temperature-dependent behavior electron emission is not well understood [70]; knowledge of that behavior would provide useful insight for future charging studies. Preliminary results for Al_2O_3 from this study indicate that the electron emission does not depend as strongly on temperature as the Arrhenius-like behavior of conductivity. Experiments focused on determining the temperature-dependent dark current and radiation-induced conductivities and related electrical properties of Al_2O_3 and PBN will further enhance the integrity of these simulations. Some of these data are available in the literature [30,43] and were used for this study. However, measurement of the exact candidate materials, including any variations due to processing technique and/or bakeout or thermal annealing, is desirable.

IV. Results and Discussion

A. Charging Analyses and Results

We present here the results of NASCAP-2K charging simulations for the Solar Probe spacecraft for two different candidate heat shield coatings (Al_2O_3 and PBN) over a CC base. For each coating, simulations were performed for a variety of radiation environments: for the estimated Jovian environment corresponding to 12 Jovian radii (R_J), for two points in deep space (2.5 and 5.0 AU), and for several near-solar locations (0.5, 0.4, 0.3, 0.2, 0.1 AU and $4R_S$).

Equilibrium charging is determined by the balance between charge accumulation (which increases with higher incident currents at closer orbital distances) and charge dissipation due to charge transport (which increases at higher temperatures and higher dose rates at closer orbital distances). The effects of the relative contributions from charge accumulation and dissipation are discussed further in Sec. IV.B. Changes in charge dissipation (conduction) mechanisms with temperature or dose rate also affect the equilibrium charge conditions. Estimated dark current conductivity, RIC, and total conductivity of Al_2O_3 as functions of the orbital distance from the sun and the heat shield temperature are plotted in Fig. 5. For estimates of both Al_2O_3 and PBN, at closer orbital distances (higher temperatures), conductivity is dominated by dark current conductivity despite the increased flux. Beyond ~0.6 AU, RIC becomes the dominant conduction mechanism, despite solar radiation and plasma dose rates that decrease with increasing distance approximately as r^{-2}. This results from a steeper temperature dependence of the Arrhenius dark current conductivity model [see Eq. (4)] than the power law temperature behavior for RIC [see Eq. (5) and Table 3]. Errors in the simulated surface voltages shown in Tables 4 and 5 were determined by varying resistivity, $\delta_{\max}$, plasma density, and electron temperature, with the resulting errors added in quadrature. There are large variations in reported resistivity versus temperature data for Al_2O_3 [32,35,71] and PBN [72,73]. This results in significant differences in the absolute values of surface voltages predicted by NASCAP modeling and constitutes one of the largest uncertainties in the potentials reported in Tables 4–6 and Figs. 6–8.

In addition, the precise solar absorptivity-to-infrared emissivity ratio ($\alpha_S/\varepsilon_{\text{IR}}$) of the coatings will depend on the method of application and on their response to the space environment. The value of $\alpha_S/\varepsilon_{\text{IR}}$ determines the temperature on the surface of the coating, such that higher values of $\alpha_S/\varepsilon_{\text{IR}}$ lead to higher surface temperatures [74]. Because resistivity is inversely related to surface temperature, higher values of $\alpha_S/\varepsilon_{\text{IR}}$ will lead to lower resistivities. Further, the magnitude of the photoemission current is proportional to the fraction of incident VIS/UV light absorbed (e.g., α_S); lower values of α_S will therefore lead to less positive charging. Therefore, results for the near-sun cases are presented for two different values of $\alpha_S/\varepsilon_{\text{IR}}$, since those values can be expected to lead to significantly different resistivities and therefore different charging behavior. The lower value ($\alpha/\varepsilon = 0.2$) is advantageous to the mission as a whole, leading to a lower overall spacecraft temperature, while the higher value ($\alpha_S/\varepsilon_{\text{IR}} = 0.6$) may be more realistic [3]. The values of the materials' electron emission, electron transport and related properties (many as a function of heat shield temperature) used in the simulations at different trajectory points were detailed in Sec. III. Charging results are summarized in Tables 4 and 5, with error bars given in parentheses in the final two columns. These reported error values represent the maximum deviation of the surface potentials from the nominal values.

B. Discussion of Charging Analyses Results

There are two primary concerns for Solar Probe charging; therefore the standard for success differs depending on where the spacecraft is located. For trajectory points at which Solar Probe was not planned to perform science operations (nominally, >0.3 AU), the main concern is to avoid elevated surface charging levels that may result in an arcing event. (As noted in Sec. I, deep dielectric charging is not considered here.) This condition is satisfied for Al_2O_3 and PBN coatings at both $\alpha/\varepsilon = 0.2$ or $\alpha/\varepsilon = 0.6$ for the deep-space and

Table 4 Charging results for an alumina-coated heat shield

Environment		Minimum potential, V		Maximum potential, V		Differential potential, V	
		$\alpha/\varepsilon = 0.6$	$\alpha/\varepsilon = 0.2$	$\alpha/\varepsilon = 0.6$	$\alpha/\varepsilon = 0.2$	$\alpha/\varepsilon = 0.6$	$\alpha/\varepsilon = 0.2$
	$4R_S$	3.8		3.8		0.0 (−0.0, +0.0)	
	0.1 AU	5.3	5.3	5.3	5.3	0.0 (−0.0, +0.0)	0.0 (−0.0, +0.0)
	0.2 AU	5.3	5.3	5.3	5.6	0.0 (−0.0, +0.0)	0.3 (−0.3, +1.5)
	0.3 AU	5.4	4.2	5.4	7.4	0.0 (−0.0, +0.1)	3.2 (−2.5, +5.3)
	0.4 AU	5.4	−8.5	5.5	6.7	0.1 (−0.1, +0.9)	15.1(−8.9, +30)
Near sun	0.5 AU	5.2	−31.1	6.1	6.1	0.9 (−0.8, +2.8)	37.2 (−25, +35)
Deep	2.5 AU	−76.4		8.1		84.4 (−21, +19)	
Space	5.0 AU	−41.2		7.8		49.0 (−10, +4.3)	
Jovian	$12R_J$	0.2		4.1		3.9 (−0.4, +11)	

Table 5 Charging results for a PBN-coated heat shield

Environment		Minimum potential, V		Maximum potential, V		Differential potential, V	
		$\alpha/\varepsilon = 0.6$	$\alpha/\varepsilon = 0.2$	$\alpha/\varepsilon = 0.6$	$\alpha/\varepsilon = 0.2$	$\alpha/\varepsilon = 0.6$	$\alpha/\varepsilon = 0.2$
	$4R_S$	3.9		3.9		0.0 (−0.0, +0.0)	
	0.1 AU	1	0.9	9.8	10	8.8 (−2.2, +1.4)	9.1 (−0.9, +1.5)
	0.2 AU	0.2	0.2	10.5	10.5	10.3 (−13.5, +55.4)	10.3 (−0.8, +72.5)
	0.3 AU	−62.2	−81.8	7.5	−6.2	69.7 (−74.4, +39.0)	75.6 (−76.3, +66.9)
	0.4 AU	−59.4	−74.3	8	−5.5	67.4 (−37.9, +27.2)	68.8 (−27.7, +43.7)
Near sun	0.5 AU	−53	−61.1	7.7	7	60.7 (−33.7 +22.7)	68.1 (−6.5, +33.8)
	2.5 AU	−6.9		6.6		13.5 (−4.7, +8.6)	
Deep space	5.0 AU	−1.9		7.8		9.7 (−0.5, +4.9)	
Jovian	$12R_J$	1.3		3.3		2.0 (−1.7, +1.7)	

Table 6 Resistivities of alumina for different resistivity reduction factors

	99.9% Alumina	10 × Reduction	100 × Reduction	1000 × Reduction	10, 000 × Reduction
Resistivity at 0.3 AU temperature, Ω-cm	3×10^{11}	3×10^{10}	3×10^{9}	3×10^{8}	3×10^{7}
Resistivity at Room-Temperature, Ω-cm	3×10^{13}	3×10^{12}	3×10^{11}	3×10^{10}	3×10^{9}
Maximum potential, V	7.4	6.0	5.5	5.4	5.4
Differential potential, V	3.24	0.73	0.10	0.01	0.001

Jovian cases; the minimum, maximum, and differential potentials remain under 100 V for 0.4 AU, 0.5 AU, 2.5 AU, 5.0 AU and $12R_J$. All nominal charging results in Tables 4 and 5 showed potentials to be below an engineering threshold for damage of electronics that was estimated as 100 V [1].

For the near-solar cases inside of 0.3 AU where science operations were planned, the situation is more complicated; this is illustrated in Fig. 6 that shows differential potential as a function of distance from the sun. While arcing is still to be avoided in this regime, the main concern is that the spacecraft potential could interfere with science data collection by deflecting the very particles that Solar Probe mission would measure. For an Al_2O_3 coating at either $\alpha/\varepsilon = 0.2$ or $\alpha/\varepsilon = 0.6$, all absolute potentials are between 4 and 7 V and all differential voltages are <3 V. Higher α/ε ratios for Al_2O_3 produce the lowest absolute and differential potentials. By contrast, for PBN both absolute and differential voltages are substantially elevated, reaching magnitudes of >80 V. For science operations concerns in near-solar cases, Al_2O_3 coatings offer a clear advantage over PBN and BaZP.

All absolute and differential potentials exhibit a pronounced peak between 0.2 and 2 AU. These potential extrema result from a competition between two contributions that are functions of distance from the sun: 1) increased charging due to larger solar radiation and plasma fluxes that increase with decreasing distance as r^{-2}, and 2) increased charge transport due to the enhanced thermal and radiation-induced conduction from the increase in absorbed thermal and radiation energies.

It can also be seen in Fig. 6 that potential difference is more for the $\alpha/\varepsilon = 0.2$ simulations, as a result of the lower temperatures for the $\alpha/\varepsilon = 0.2$ heat shields that result in lower conduction and charge dissipation. All absolute potentials for both Al_2O_3 and PBN, with the exception of the maximum potential for $\alpha/\varepsilon = 0.6$, exhibit a

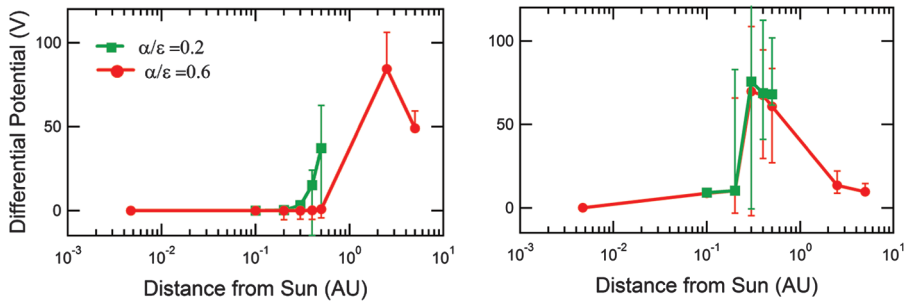

Fig. 6 Dependence of the differential surface potential on distance from the sun for the Solar Probe spacecraft: a) Al_2O_3-coated heat shield, and b) PBN-coated heat shield.

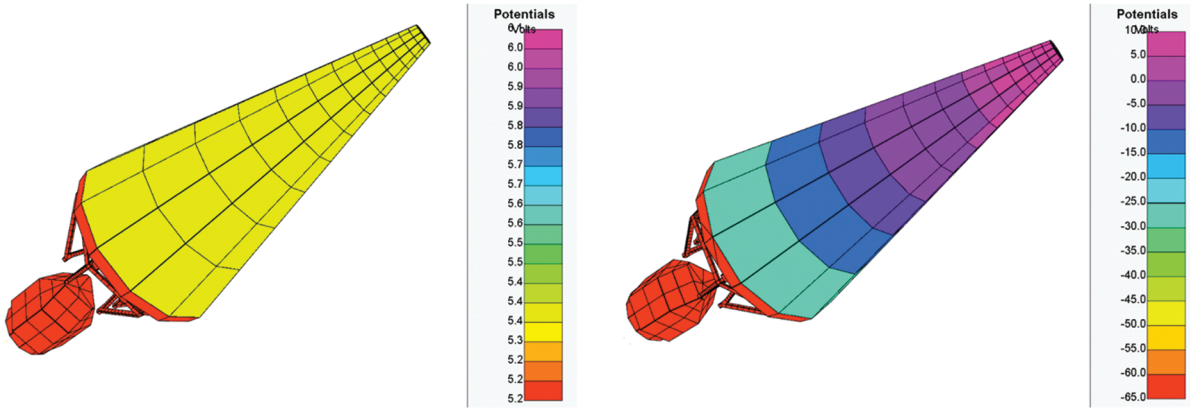

a) b)

Fig. 7 Charging of Solar Probe spacecraft at 0.3 AU with $\alpha_S/\varepsilon_{IR} = 0.6$: a) alumina-coated heat shield, and b) PBN-coated heat shield.

transition from positive charging nearer to the sun, where photoemission dominates to negative charging at more distant trajectory points.

Note the smooth potential contours along the length of the spacecraft in the absolute potential profiles of the spacecraft in Fig. 7. These results show differential charging of <1 V for alumina and <70 V for PBN from cone tip to the bus. In the case of PBN, the potential gradient is likely due to the electrically insulating ceramic cone photoemitting while the instrument bus is shaded; lack of electrical conduction between the two (due to the relatively high resistivity of the ceramic at this point in the trajectory) results in the potential differential.

It should be noted that although the error estimates for the differential potential are fairly large for some trajectory positions (0.2–2.5 AU), this reflects the sensitivity of the potential to the distance from the sun in that range. This effect can be seen in Fig. 6 and Tables 4 and 5; for both Al_2O_3 and PBN coatings, the spacecraft transitions quickly from differential potentials in the single digits to potentials of tens of volts as the distance from the sun increases, with a critical point in the region of 0.2–2 AU. Errors in the various input parameters have effects of varying degrees on the results; for example, as expected, the resistivity has a large impact on the spacecraft potential, whereas the impact of the plasma densities is relatively small [48]. Consequently, errors in the input parameters (resistivity, electron emission, particle energies, and particle densities) will have the effect of shifting the potential peaks within that range. To look at the situation from another perspective, one might say that the transition point is 0.3 ± 0.2 AU for the case of a PBN coating.

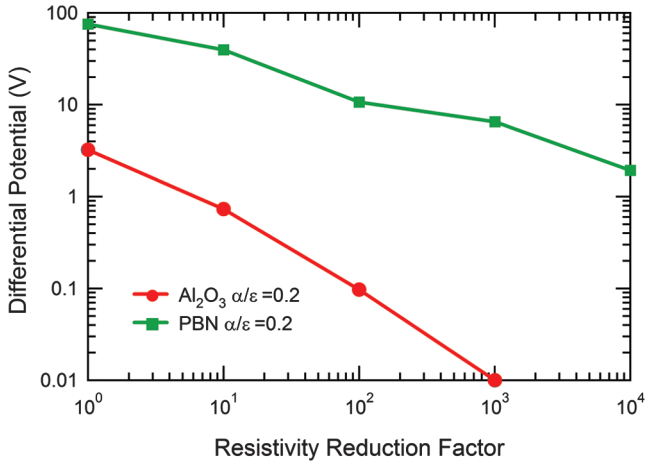

Fig. 8 Reductions in differential charging when the coating resistivity is lowered via doping. Results shown here are for Al_2O_3 and PBN with $\alpha_S/\varepsilon_{IR} = 0.2$ at 0.3 AU, where maximum differential charging is found.

C. Mitigation of Charge

Although the charging of the ceramic-coated heat shield is far from the damage threshold and generally low in the region of science operations, it may be necessary to further mitigate the charging characteristics of the coating to meet the stringent requirements for a Solar Probe mission. One option to mitigate charging is to lower the resistivity of the ceramic coatings such that they will be more conductive at the nominal start-of-science point.

Lowering the resistivity of the ceramic coating could also be accomplished by doping the coatings, that is, by adding small quantities of impurities to the ceramic material, thereby lowering its electrical resistivity (both dark current conductivity and RIC would be affected by doping). An analysis of the impact of doping the coating materials on charging indicates that charging can be significantly mitigated in the vicinity of 0.3 AU. The improvements to differential charging that lowered dark current resistivity can provide are illustrated for alumina and PBN in Fig. 8 and Table 6. A reduction of the dark resistivity by a factor of 100, for example, lowers the maximum spacecraft potential difference at 0.3 AU from ~3 V to ~0.1 V for alumina and from ~75 V to 10 V for PBN.

Controlled resistivity alumina with room-temperature resistivities in the range required for a $10,000\times$ reduction in resistivity is commercially available. Examples include 97% pure alumina with room-temperature resistivity of 6×10^{12} Ω-cm and 96% pure alumina with room-temperature resistivity of 5×10^{11} Ω-cm [75]. In general, the amount and type of doping required to modify conduction by these amounts does not appreciably alter the optical properties, in particular $\alpha_S/\varepsilon_{IR}$.

Another possibility is to mix the ceramic coating with low concentrations of dispersed conductive nanostructures, as has been done for polymeric spacecraft materials such as Kapton loaded with graphitic carbon particles (black Kapton [Dupont]) or carbon nanotubes. Because of the high aspect ratio of nanostructures such as carbon nanotubes (typically ~1 mm long and ~1 nm wide), only a relatively low concentration of these nanostructures is required to achieve percolated conductivity and a commensurate reduction in resistivity. For example, Ahmad et al. [76] found that 1–2% (by volume) carbon–nanotube-doped alumina decreased resistivity by 10 orders of magnitude. The experiments by Ahmad's group were performed at room temperature; however, other studies of the behavior of carbon nanotubes at high temperatures have demonstrated thermal stability up to 2000°C [77]. Also, even at these low nanostructure concentrations, optical and thermal properties may be affected. For example, addition of carbon can blacken a material and increase $\alpha_S/\varepsilon_{IR}$, thereby increasing the material equilibrium temperature and hence increasing the conductivity. It is conceivable that carbon-induced modifications to $\alpha_S/\varepsilon_{IR}$ could warm the cone materials enough in deep-space and Jovian environments to better dissipate surface and deep dielectric charge. Alternately, increasing α_S also increases photoyield and hence positive charging.

Enhanced conductivity will certainly act to reduce differential charging. In most cases investigated here the heat shield and spacecraft bus charge to opposite polarities, so that enhanced charge transport will result in charge recombination and a reduced overall absolute charge. Under these circumstances, the overall absolute charge could be further reduced to near zero potential by adjusting the relative areas of positive and negative charging surfaces.

V. Conclusions

We have presented analyses of the behavior of ceramic materials in space environments, specifically as they pertain to the 2005 Solar Probe mission concept. We have used a combination of radiation environment estimation, material property measurements, and finite element-based simulations to evaluate the charging response of two ceramic materials, alumina and pyrolytic boron nitride. Although the electrical properties of such materials present a challenge to their use in space, we find that differential surface charging, though significant, is not severe enough to cause a risk of discharge. The degree of differential surface charging depends strongly on temperature and on the materials used. The differential surface charging for this Al_2O_3 coated spacecraft ranges from 0 to 85 V along the mission trajectory, with appreciable difference evident between $\alpha_S/\varepsilon_{IR}$ values. At distances of less than 0.4 AU Al_2O_3 also exhibits a substantially lower range of absolute charging than PBN. The charging of the ceramic coatings could interfere with instrument operations and cause measurement contamination. Taken together, the measurements of materials properties strongly suggest that Al_2O_3 ceramic coatings would be preferable to either PBN or BaZP coatings based on spacecraft charging concerns.

Absolute and differential surface charging are found to depend strongly on temperature through increased conductivity at higher temperatures and on radiation flux through enhanced charge accumulation and radiation-induced conductivity. As the spacecraft approaches the sun, the competition between increased charge dissipation at higher temperatures and increased charge accumulation at higher fluxes leads to a maximum in differential charging between 0.2 and 2 AU.

Future investigations should be directed toward mitigation of the charging behavior as discussed in the paper, which could include doping with conductors or with carbon nanotubes. Further measurements of temperature-dependent materials properties, including dark current and radiation-induced conductivities, electron emission, and photoyields, are necessary to refine charging simulations. The possible effects of deep dielectric charging in the Jovian and near-sun environments should also be considered more fully.

Acknowledgments

The authors are grateful to Jerold Emhoff, Thomas Wolf, David Drewry, Don King, Douglas Mehoke, and Kenneth Potocki of Johns Hopkins University Applied Physics Laboratory for their inputs and helpful discussions, to E. C. Sittler of NASA-Goddard Space Flight Center for assistance with radiation environment definition, and to the Solar Probe Science and Technology Definition team (led by D. J. McComas of Southwest Research Institute) for their helpful discussions and support. We appreciate the NASA support provided by H. Maldonado of the NASA–Goddard Space Flight Center under contract NAS5-01072 for the engineering trade studies. We also acknowledge J. C. Sommerer, J. J. Suter, V. R. McCrary, and R. McNutt (all of JHU/APL) for their continuing support through Johns Hopkins University Applied Physics Laboratory Independent Research and Development funding for the development of the fundamental material technology.

References

[1] NASA, "Solar Probe: Report of the Science and Technology Definition Team," NASA TM-2005-212786, 2005, http://solarprobe.gsfc.nasa.gov/SolarProbe_STDT2005.pdf.

[2] McComas, D. J., Velli, M., and Lewis, W. S., "Solar Probe: Humanity's First Visit to a Star," *Solar Wind 11/SOHO 16: Connecting Sun and Heliosphere*, European Space Agency, Noordwijk, Netherlands, 2005, pp. 279–286.

[3] "Solar Probe Thermal Protection System Risk Mitigation Study: FY 2006 Final Rept.," Johns Hopkins Univ. Applied Physics Lab., Rept. 06-05015-1, 2007, http://solarprobe.gsfc.nasa.gov/SP_RMStudy_HiRes.pdf.

[4] Drewry, D. G., King, D. E., Mehoke, D. S., Potocki, K. A., Sample, J. L., Clemons, D. E., Caruso, K. S., Donegan, M. M., Wolf, T. D., Mattix, M. P., Thomas, M. E., and Emhoff, J. W., "Passive Optical-Based Thermal Management Approach for Spacecraft Operating in the Near Solar Environment," *8th AIAA/ASME/ASCE/AHS/ASC Structures, Structural Dynamics, and Materials Conference, Vol. 6*, AIAA, Reston, VA , Paper 20191-4344, 2007, pp. 5897–5905.

[5] "Solar Probe Plus: Rept. of the Science and Technology Definition Team," NASA, Rept. TM- 2008-214161, 2008, http://solarprobe.jhuapl.edu/mission/docs/SolarProbe_STDT2008.pdf.

[6] "Solar Probe and Mission Engineering Study Rept.," Johns Hopkins Univ. Applied Physics Lab., 2008, http://solarprobe.jhuapl.edu/mission/docs/SolarProbeME.pdf.

[7] Scime, E. E., Phillips, J. L., and Bame, S. J., "Effects of Spacecraft Potential on Three-Dimensional Electron Measurements in the Solar Wind," *Journal of Geophysical Research*, Vol. 99, No. A8, 1994, pp. 14,769–14,776. doi:10.1029/94JA00489

[8] Mandell, M. J., Davis, V. A., and Cooke, D. L., "NASCAP-2K Spacecraft Charging Code Overview," *IEEE Transactions on Plasma Science*, Vol. 34, No. 5, 2006, pp. 2084–2093. doi:10.1109/TPS.2006.881934

[9] Mandell, M., Katz, I., and Hilton, J. M., "NASCAP-2K Spacecraft Charging Models: Algorithms and Applications," *Spacecraft Charging Technology, Proceedings of the Seventh International Conference*, edited by R. A. Harris, European Space Agency, Noordwijk, Netherlands, SP-476, 2001, pp. 1–10.

[10] Davis, V. A., Mandell, M. J., and Gardner, B. M., "Validation of NASCAP-2K Spacecraft-Environment Interactions Calculations," *Proceedings of the 8th Spacecraft Charging Conference*, Huntsville, AL, 2004, http://hdl.handle.net/2060/20040111077.

[11] Potocki, K. A., Eng, D. A., and McComas, D. J., "Solar Probe Engineering Concept," *Solar Wind 11/SOHO 16: Connecting Sun and Heliosphere*, European Space Agency, Noordwijk, Netherlands, 2005, pp. 697–700.

[12] McComas, D. J., Bame, S. J., and Barraclough, B. L., "Ulysses' Return to the Slow Solar Wind," *Geophysical Research Letters*, Vol. 25, No. 1, 1998, pp. 1–4. doi:10.1029/97GL03444

[13] Maurice, S., Sittler, E. C., Cooper, J. F., Mauk, B. H., Blanc, M., and Selenick, R. S., "Comprehensive Analysis of Electron Observations at Saturn: Voyager 1 and 2," *Journal of Geophysical Research*, Vol. 101, No. A7, 1996, pp. 15,211–15,232. doi:10.1029/96JA00765

[14] Dennison, J. R., Alec Sim, and Clint Thomson, "Evolution of the Electron Yield Curves of Insulators as a Function of Impinging Electron Fluence and Energy," *IEEE Transaction on Plasma Science*, Vol. 34, No. 5, Oct. 2006, pp. 2204–2218. doi:10.1109/TPS.2006.883398

[15] Schwenn, R., Montgomery, M. D., Rosenbauer, H., Miggenrieder, H., Muehlhaeuser, K. H., Bame, S. J., Feldman, W. C., and Hansen, R. T., "Direct Observation of the Latitudinal Extent of a High-Speed Stream in the Solar Wind," *Journal of Geophysical Research*, Vol. 83, No. A3, 1978, pp. 1011–1017. doi:10.1029/JA083iA03p01011

[16] Bame, S. J., McComas, D. J., Barraclough, B. L., Phillips, J. L., Sofaly, K. J., Chavez, J. C., Goldstein, B. E., and Sakurai, R. K., "The ULYSSES Solar Wind Plasma Experiment," *Astronomy and Astrophysics Supplement Series*, Vol. 92, No. 2, 1992, pp. 237–265.

[17] Maksimovic, M., Gary, S. P., and Skoug, R. M., "Solar Wind Electron Suprathermal Strength and Temperature Gradients: Ulysses Observations," *Journal of Geophysical Research*, Vol. 105, No. A8, 2000, pp. 18,337–18,350. doi:10.1029/2000JA900039

[18] Guhathakurta, M., Sittler, E. C., and Ofman, L., "Semiempirically Derived Heating Function of the Corona Heliosphere During the Whole Sun Month," *Journal of Geophysical Research*, Vol. 111, No. A11, 2006, p. A11215. doi:10.1029/2006JA011931

[19] Sittler, E. C. Jr., and Scudder, J. D., "An Empirical Polytrope Law for Solar Wind Thermal Electrons Between 0.45 and 4.76 AU—Voyager 2 and Mariner 10," *Journal of Geophysical Research*, Vol. 85, No. A10, 1980, pp. 5131–5137.

doi:10.1029/JA085iA10p05131
[20] Sittler, E. C., and Strobel, D. F., "Ion Plasma Torus Electrons: Voyager 1," *Journal of Geophysical Research*, Vol. 92, No. A6, 1987, pp. 5741–5762.
doi:10.1029/JA092iA06p05741
[21] Scudder, J. D., Sittler, E. C., and Bridge, H. S., "A Survey of the Plasma Electron Environment of Jupiter - A View from Voyager," *Journal of Geophysical Research*, Vol. 86, No. A10, 1981, pp. 8157–8179.
doi:10.1029/JA086iA10p08157
[22] Paranicas, C., Carlson, R. W., and Johnson, R. E., "Electron Bombardment of Europa," *Geophysical Research Letters*, Vol. 28, No. 4, 2001, pp. 673–676.
doi:10.1029/2000GL012320
[23] Paranicas, C., Ratliff, J. M., Mauk, B. H., Cohen, C., and Johnson, R. E., "The Ion Environment Near Europa and its Role in Surface Energetics," *Geophysical Research Letters*, Vol. 29, No. 5, 2002, pp. 18-1–18-4.
doi:10.1029/2001GL014127
[24] Mauk, B. H., Mitchell, D. G., McEntire, R. W., Paranicas, C. P., Roelof, E. C., Williams, D. J., Krimigis, S. M., and Lagg, A., "Energetic Ion Characteristics and Neutral Gas Interactions in Jupiter's Magnetosphere," *Journal of Geophysical Research*, Vol. 109, No. A9, 2004, pp. 1–24.
doi:10.1029/2003JA010270
[25] Kivelson, M. G., Bagenal, F., Kurth, W. S., Neubauer, F. M., Paranicas, C., and Saur, J., "Magnetospheric Interactions with Satellites," in *Jupiter. The Planet, Satellites and Magnetosphere*, edited by F. Bagenal, T. E. Dowling, and W. B. McKinnon, Cambridge Univ. Press, Cambridge, England 2004, pp. 513–536.
[26] Cooper, J. F., Johnson, R. E., Mauk, B. H., Garrett, H. B., and Gehrels, N., "Energetic Ion and Electron Irradiation of the Icy Galilean Satellites," *Icarus*, Vol. 149, No. 1, 2001, pp. 133–159.
doi:10.1006/icar.2000.6498
[27] Hastings, D., and Garrett, H., *Spacecraft–Environment Interactions*, Cambridge Press, New York, 1996.
doi:10.2277/0521607566
[28] Dennison, J. R., Alec Sim, Jerilyn Brunson, Steven Hart, Jodie Gillespie, Justin Dekany, Charles Sim and Dan Arnfield, "Engineering Tool for Temperature, Electric Field and Dose Rate Dependence of High Resistivity Spacecraft Materials," *Proceedings of the 47th American Institute of Aeronautics and Astronomics Meeting on Aerospace Sciences*, AIAA, Reston, VA, Paper 2009-0562, 2009.
[29] Thomson, C. D., Zavyalov, V., Dennison, J. R., and Corbridge, J., "Electron Emission Properties of Insulator Materials Pertinent to the International Space Station," *Proceedings of the 8th Spacecraft Charging Technology Conference*, Huntsville, AL, 2004, http://hdl.handle.net/2060/20040111072.
[30] Dennison, J. R., Chang, W. Y., Nickles, N., Kite, J., Thomson, C. D., Corbridge, J., and Ellsworth, C., "Electronic Properties of Materials with Application to Spacecraft Charging, Part III: Materials Reports," NASA Space Environments and Effects Program Grant, Sept. 2002.
[31] Drewry, D., King, D., Sample, J., Clemons, D., Caruso, K., Potocki, K., Eng, D., Mehoke, D., Mattix, M., Thomas, M., and Nagle, D., "Spacecraft Thermal Management Via Control of Optical Properties in the Near Solar Environment," *Advanced Ceramic Coatings and Interfaces: Ceramic Engineering and Science Proceedings*, Vol. 27, No. 3, 2007, pp. 233–244.
doi:10.1002/9780470291320.ch22
[32] Tillar Shugg, W., "The Guide to Plastics," *Handbook of Electrical and Electronic Insulating Materials*, 2nd ed., McGraw–Hill, New York, 1970.
[33] CVT GmbH and Company KG, "PBN Materials" 2009, http://www.cv-technology.com/i_technology_cvd.html, Accessed 8/25/2009.
[34] Wesgo Ceramics Hayward, "Controlled Resistivity Alumina," 2007, accessed 06/15/2007. Available at http://www.wesgo.com/resist.htm.
[35] Morrell, R., "Handbook of Properties of Technical and Engineering Ceramics, Part 2: Data Reviews; Section I: High-Alumina Ceramics," Her Majesty's Stationery Office, London, pp. 1–255, 1987.
[36] Chang, W. Y., Dennsion, J. R., and Parker, J., "Measurements of Electronic Properties of Conducting Spacecraft Materials with Application to the Modeling of Spacecraft Charging," *Proceedings of the 38th American Institute of Aeronautics and Astronomics Meeting on Aerospace Sciences*, AIAA, Reston, VA, Paper 2000-0870, 2000.
[37] Wintle, H. J., "Conduction Processes in Polymers," *Engineering Dielectrics–Volume IIA: Electrical Properties of Solid Insulating Materials: Molecular Structure and Electrical Behavior, American Society for Testing and Materials*, edited by R. Bartnikas, American Society for Testing and Materials, Philadelphia, 1983.
[38] Dennison, J. R., Thomson, C. D., Kite, J., Zavyalov, V., and Corbridge, J., "Materials Characterization at USU: Facilities and Knowledgebase of Electronic Properties Applicable to Spacecraft Materials," in *Proceedings of the 8th Spacecraft. Charging Technology Conference*, Huntsville, AL, 2004, http://hdl.handle.net/2060/20040111058.
[39] Chang, W. Y., Dennison, J. R., Nickles, N., and Davies, R. E., "Utah State University Ground-based Test Facility for Study of Electronic Properties of Spacecraft Materials," *Proceedings of the 6th Spacecraft Charging Technology Conference*, Air Force Research Lab. Science Center, Hanscom Air Force Base, MA, 2000.
[40] Hoffmann, R., and Dennison, J. R., "Electron-Induced Electron Yields of Uncharged Insulating Materials," *Proceedings of the 10th Spacecraft Charging Technology Conference*, Centre National d'Études Spatiales, Biarritz, France, 2007.
[41] Hoffmann, R., Dennison, J. R., Thomson, C. D., and Albresten, J., "*Low-Fluence Electron Yields of Highly Insulating Materials*," *IEEE Trans. on Plasma Science*, Vol. 36, No. 5, 2008, pp. 2238–2245.
[42] Purvis, C., Garrett, H. B., Whittlesey, A. C., and Stevens, N. J., "Design Guidelines for Assessing and Controlling Spacecraft Charging Effects," NASA Scientific and Technical Information Branch, Technical Paper 2361, 1984.
[43] Dawson, P. H., "Secondary Electron Emission Yields of Some Ceramics," *Journal of Applied Physics*, Vol. 37, No. 9, 1966, p. 3644.
doi:10.1063/1.1708934
[44] Sample, J. L., Donegan, M., Wolf, T., Drewry, D., and Mehoke, D., "Charging of Ceramic Coatings in Space," *48th AIAA/ASME/ASCE/AHS/ASC Structures, Structural Dynamics, and Materials Conference*, Vol. 6, AIAA, Reston, VA, 2007, pp. 5889–5896.
[45] Dietz, L. A., and Sheffield, J. C., "Secondary Electron Emission Induced by 5-30-keV Monatomic Ions Striking Thin Oxide Films," *Journal of Applied Physics*, Vol. 46, No. 10, 1975, p. 4361.
doi:10.1063/1.321463
[46] Feuerbacher, B., and Fitton, B., "Experimental Investigation of Photoemission from Satellite Surface Materials," *Journal of Applied Physics* Vol. 41, No. 4, 1972, p. 1536.
doi:10.1063/1.1661362
[47] Grard, Rejean, J. L., "Properties of the Satellite Photoelectron Sheath Derived from Photoemission Laboratory Measurements," *Journal of Geophysical Research*, Vol. 78, No. 16, 1973, p. 2885.
doi:10.1029/JA078i016p02885
[48] Dennison, J. R., Hoffmann, R. C., and Abbott, J., "Triggering Threshold Spacecraft Charging with Changes in Electron Emission from Materials," *Proceedings of the 45th American Institute of Aeronautics and Astronomics Meeting on Aerospace Sciences*, AIAA, Paper 2007-1098, p. 16, Reno, NV, January, 10, 2007.
[49] Lai, S. T., and Tautz, M., "Aspects of Spacecraft Charging in Sunlight," *IEEE Transactions on Plasma Science*, Vol. 34, No. 5, 2006, p. 2053.
doi:10.1109/TPS.2006.883362
[50] Chantler, C. T., Olsen, K., Dragoset, R. A., Chang, J., Kishore, A. R., Kotochigova, S. A., and Zucker, D. S., "X-Ray Form Factor, Attenuation and Scattering Tables (Version 2.1)," National Institute of Standards and Technology, Gaithersburg, MD, Aug. 2009, http://physics.nist.gov/ffast. Originally published as Chantler, C. T., *Journal of Physical and Chemical Reference Data*, Vol. 29, No. 4, 2000, pp. 597–1048.
doi:10.1063/1.1321055;
[51] National Institute of Standards and Technology, "ESTAR, Stopping Power and Range Tables for Electrons [NIST database]," 2009, http://units.nist.gov/PhysRefData/Star/Text/ESTAR.html, accessed 8/25/2009.
[52] Momentive Performance Materials, "Pyrolytic Boron Nitride (PBN) Materials," 2009, accessed 8/25/2009. Available at http://www.advceramics.com/products/pyrolytic_bn/.
[53] Yoshimura, M., and Bowen, H., "Electrical Breakdown Strength of Alumina at High Temperatures," *Journal of the American Ceramic Society*, Vol. 64, No. 7, 1981, pp. 404–410.
doi:10.1111/j.1151-2916.1981.tb09879.x
[54] Sabuni, H., and Nelson, J. K., "The Electrical Strength of Copolymers," *Journal of Materials Science*, Vol. 12, No. 12, 1977, pp. 2435–2440.
doi:10.1007/BF00553930
[55] Crine, J.-P., Parpal, J.-L., and Dang, C., "A New Approach to the Electric Aging Of Dielectrics," Electrical Insulation and Dielectric Phenomena, IEEE Publications, Piscataway, NJ, 29 Oct.-2–Nov. 1989, pp. 161-167.
doi:10.1109/CEIDP.1989.69540
[56] Wintle, H. J., "Conduction Processes in Polymers," in *Engineering Dielectrics–Volume IIA: Electrical Properties of Solid Insulating Materials: Molecular Structure and Electrical Behavior, American Society for Testing and Materials*, edited by R. Bartnikas, American Society for Testing and Materials, Philadelphia, 1983.
[57] Ashcroft, N. W., and Mermin, N. D., *Solid State Physics*, 1st ed.,

Rinehart and Winston, New York,1976.
[58] Rose, A., "An Outline of Some Photoconductive Processes," *RCA Review*, Vol. 12, No. 3, 1951, p. 362.
[59] Fowler, J. F., "X-Ray Induced Conductivity in Insulating Materials," *Proceedings of the Royal Society of London, Series A: Mathematical and Physical Sciences*, Vol. 236, No. 1207, 1956, pp. 464–480. doi:10.1098/rspa.1956.0149
[60] Dennison, J. R., Jodie Gillespie, Joshua Hodges, Hoffmann, R. C., Abbott, J., Alan W. Hunt, and Randy Spalding, "Radiation Induced Conductivity of Highly Insulating Spacecraft Materials," *Application of Accelerators in Research and Industry*, American Institute of Physics Conference Proceedings Series, Vol. 1099, edited by Floyd D. McDaniel, and Barney L. Doyle, American Institute of Physics, Melveille, NY, 2009, pp. 203–208.
[61] Klaffky, R., Rose, B., Goland, A. N., and Dienes, G. J., "Radiation-Induced Conductivity of Al_2O_3: Experiment and Theory," *Physical Review B*, Vol. 21, No. 8, 1980, pp. 3610–3634. doi:10.1103/PhysRevB.21.3610
[62] Jennifer A. Roth, Ryan Hoffmann, Dennison, J. R., and Tippetts, J. R., "Effects of Radiation Induced Conductivity on Electrostatic Discharge in Insulating Materials," *Proceedings of the 1st AIAA Atmospheric and Space Environments Conference*, AIAA, Reston, VA, Paper 2009-3527, 2009.
[63] Reimer, L., *Scanning Electron Microscopy*, Springer–Verlag, Berlin, 1985.
[64] Garrett, H. B., and DeForest, S. E., "An Analytic Simulation of the Geosynchronous Plasma Environment," *Planetary and Space Science*, Vol. 27, No. 8, 1979, pp. 1101-09.
[65] Somorjai, G. A., *Chemistry in Two Dimensions: Surfaces*, Cornell Univ., Ithaca, NY, 1981.
[66] Penn, D. R., "Electron Mean Free Paths for Free Electron-Like Materials," *Physical Review B: Solid State*, Vol. 13, No. 12, 1976, pp. 5248–5254.
[67] Powell, C. J., and Jablonski, A., NIST Electron Inelastic-Mean-Free-Path Database, Version 1.1, National Institute of Standards and Technology, Gaithersburg, MD (2000).
[68] Laurer, J. L., and Shohet, J. L., "Surface Potential Measurements of Vacuum Ultraviolet Irradiated Al2O3, Si3N4, and SiO2," *IEEE Transactions on Plasma Science*, Vol. 33, No. 2, 2005, pp. 248–249. doi:10.1109/TPS.2005.845307
[69] Upadhyaya, G. S., Kruger, J. B., and Shohet, J. L., "Vacuum Ultraviolet-Induced Charge Depletion in Plasma Charges Patterned-Dielectric Wafers," *Journal of Applied Physics*, Vol. 105, No. 053308, 2009. doi:10.1063/1.3088889
[70] Grais, K. I., and Bastawros, A. M., "A Study of Secondary Electron Emission in Insulators and Semiconductors," *Journal of Applied Physics*, Vol. 53, No. 7, 1982, p. 5239. doi:10.1063/1.331403
[71] Momentive Performance Materials, "Pyrolytic Boron Nitride (PBN) Materials," 2009, http://www.advceramics.com/products/pyrolytic_bn/., Accessed 8/25/2009.
[72] Wintle, H. J., "Conduction Processes in Polymers," *Engineering Dielectrics Volume IIA: Electrical Properties of Solid Insulating Materials: Molecular Structure and Electrical Behavior, American Society for Testing and Materials*, edited by R. Bartnikas, American Society for Testing and Materials, Philadelphia 1983.
[73] Ashcroft, N. W., and Mermin, N. D., *Solid State Physics*, 1st ed., Rinehart and Winston, New York, 1976.
[74] Caruso, K. S., Drewry, D. G., King, D. E., and Jones, J. S., "Heat Treatment of Plasma-Sprayed Alumina: Evolution of Microstructure and Optical Properties," *Advanced Ceramic Coatings and Interfaces II: Ceramic Engineering and Science Proceedings*, Vol. 28, No. 3, 2007, pp. 177–192.
[75] Wesgo Ceramics Hayward, "Controlled Resistivity Alumina," 2007, Available at http://www.wesgo.com/resist.htm, accessed 06/15/2007.
[76] Ahmad, K., Pan, W., and Shi, S., "Electrical Conductivity and Dielectric Properties of Multiwalled Carbon Nanotube and Alumina Composites," *Applied Physics Letters*, Vol. 89, No. 13, 2006, pp. 133122-1–133122-3. doi:10.1063/1.2357920
[77] Kim, Y. A., Muramatsu, H., Hayashi, T., Endo, M., Terrones, M., and Dresselhaus, M. S., "Thermal Stability and Structural Changes of Double-walled Carbon Nanotubes by Heat Treatment," *Chemical Physics Letters*, Vol. 398, Nos. 1–3, 2004, pp. 87–92. doi:10.1016/j.cplett.2004.09.024

I. Boyd
Associate Editor